CrossMark

electronic reprint

JOURNAL OF APPLIED CRYSTALLOGRAPHY

ISSN: 1600-5767

journals.iucr.org/j

Nested Kirkpatrick–Baez (Montel) optics for hard X-rays

Giacomo Resta, Boris Khaykovich and David Moncton

J. Appl. Cryst. (2015). **48**, 558–564

Journal of
Applied Crystallography
ISSN 1600-5767

Received 19 August 2014
Accepted 23 February 2015

Nested Kirkpatrick–Baez (Montel) optics for hard X-rays

Giacomo Resta, Boris Khaykovich* and David Moncton

Massachusetts Institute of Technology, 77 Massachusetts Avenue, Cambridge, MA 02139, USA. Correspondence e-mail: bkh@mit.edu

A comprehensive description and ray-tracing simulations are presented for symmetric nested Kirkpatrick–Baez (KB) mirrors, commonly used at synchrotrons and in commercial X-ray sources. This paper introduces an analytical procedure for determining the proper orientation between the two surfaces composing the nested KB optics. This procedure has been used to design and simulate collimating optics for a hard-X-ray inverse Compton scattering source. The resulting optical device is composed of two 12 cm-long parabolic surfaces coated with a laterally graded multilayer and is capable of collimating a 12 keV beam with a divergence of 5 mrad (FWHM) by a factor of ∼250. A description of the ray-tracing software that was developed to simulate the graded multilayer mirrors is included.

1. Introduction

Many important techniques for probing the structure and dynamics of matter (such as protein crystallography and X-ray microscopy) require extremely bright hard X-ray sources equipped with sophisticated beam-shaping optics, such as grazing-incidence focusing mirrors. In particular, Kirkpatrick–Baez (KB) optics consist of two perpendicular reflecting mirrors, bent elliptically or parabolically in one direction and positioned sequentially with respect to each other. In the case of nested KB mirrors, also known as L-shaped or Montel mirrors, the two surfaces are mounted adjacent to each other. Compared to the sequential counterpart, nested KB mirrors are more compact and are capable of higher demagnification/magnification. In addition, the two mirrors making the sequential KB optics have to be placed at different distances from the foci, meaning that their shape must be different and each one produces an image of the source with different magnification. In contrast, nested mirrors are identical. As a result, their potential applications include both laboratory and synchrotron X-ray sources.

While several papers have described the construction and testing (Honnicke *et al.*, 2011) of nested KB optics, details related to the alignment of the individual surfaces appear to be absent from the literature. As we show below, for the optimal alignment, the surfaces must deviate from the 90° orientation relative to each other. This is a result of the noncommuting nature of individual reflections from each of the surfaces composing the optics.

We derive analytic expressions to determine the correct orientation between the surfaces and confirm these expressions by ray-tracing simulations. Using these expressions, we design a Montel collimator for use with a recently proposed novel inverse Compton scattering (ICS) source (Graves *et al.*, 2014). ICS sources may provide a laboratory-size hard X-ray source with comparable brightness to the third-generation synchrotron facilities, but with an angular divergence larger than that of synchrotrons, ∼5 mrad at ∼12 keV, and with much smaller source size, ∼3 µm. Many X-ray techniques require a well collimated beam to go through perfect-crystal Si or Ge monochromators, which accept a beam divergence smaller than 100 µrad.

Therefore, we designed a set of parabolic nested KB mirrors able to collimate a beam from an ICS source, while being only 12 cm in length. For comparison, a sequential KB configuration providing a similar throughput would be approximately 31 cm in length (12 cm for the first mirror and 19 cm for the second). Other potential applications of nested KB mirrors include inelastic X-ray scattering and X-ray nanoprobes. Both techniques require focusing mirrors with performance characteristics similar to those required for the collimator described here. In the case of nanoprobes, elliptical mirrors are necessary (Liu *et al.*, 2011). In addition, neutron applications of elliptical nested KB mirrors have been recently described (Ice *et al.*, 2009; Weichselbaumer *et al.*, 2014). We believe that the methods developed in this paper could be extended to nested KB mirrors suitable for these applications.

2. General configuration

Fig. 1 illustrates the beamline configuration used to analyze the collimation setup. The source itself is located at the origin of the coordinate system and modeled as emitting a monochromatic, spatially uniform, angularly Gaussian X-ray beam with an energy of 12 keV, a radius of 2.5 µm and an FWHM divergence of 5 mrad. These parameters approximate the expected output from an inverse Compton Source (Graves *et al.*, 2009). A detector is located 10 m from the end of the optics to inspect the size and divergence of the output beam.

The collimating mirrors are two parabolic surfaces whose geometry is given by equations (1) and (2) below. Owing to constraints of the inverse Compton source, the leading edges of the mirrors are placed at 0.2 m from the source.

2.1. Parabolic surface geometry

In standard Cartesian coordinates, the geometry of parabolic nested KB mirror surfaces ($\mathbf{S}_{p1}$ and $\mathbf{S}_{p2}$) is given by

$$\mathbf{S}_{p1}(x, z) = \{\, x \quad -2[p(z+p)]^{1/2} \quad z \,\}, \tag{1}$$

$$\mathbf{S}_{p2}(y, z) = \{\, -2[p(z+p)]^{1/2} \quad y \quad z \,\}, \tag{2}$$

where p is the parabolic parameter and x, y, z span the dimensions of the optics. The focus of the mirrors coincides with the X-ray source at the origin of the coordinate system.

It is convenient to define the parabolic parameter, p, in equations (1) and (2) in terms of the y and z coordinates of the edge closest to the focus on $\mathbf{S}_{p1}$. Denoting these values by y_s and z_s, respectively, we find that

$$p = \frac{-z_s + (z_s^2 + y_s^2)^{1/2}}{2}. \tag{3}$$

The vectors normal to the surfaces in equations (1) and (2) are given by

$$\mathbf{n}_{p1}(z) = \left[\, 0 \quad \left(\frac{z+p}{z+2p}\right)^{1/2} \quad \left(\frac{p}{z+2p}\right)^{1/2} \,\right], \tag{4}$$

$$\mathbf{n}_{p2}(z) = \left[\, \left(\frac{z+p}{z+2p}\right)^{1/2} \quad 0 \quad \left(\frac{p}{z+2p}\right)^{1/2} \,\right]. \tag{5}$$

3. Perpendicular nested KB mirrors form two divergent beams

Analysis of the mirrors described by equations (1) and (2) shows that such optics cannot collimate the beam properly. Instead, the rays that traverse the optics are separated into two groups with different average divergences. This separation results in a notable angular gap in the output beam, as visible in the simulation results shown in Fig. 2.

The formation of the gap is understood with the help of geometrical optics. A divergent set of rays originating from the focal point is intercepted by the mirrors. One half of the rays will reflect from the mirror $\mathbf{S}_{p1}$, followed by $\mathbf{S}_{p2}$, while the other half will interact first with $\mathbf{S}_{p2}$ and then with $\mathbf{S}_{p1}$ (hereafter, the subscript p will be omitted for brevity). The first reflection would change the direction of a ray in one plane (see Fig. 3). Therefore, this ray will reflect from the second surface as if it were coming from a virtual source, which is different from the focal point at the origin (point P_2 in Fig. 3). Thus, half of the beam is perfectly collimated along the x axis and divergent along the y axis, while the other half is perfectly collimated along the y axis and divergent along the x axis, resulting in an angular gap.

This effect is described mathematically as follows. Consider a particle which will hit very close to the intersection between

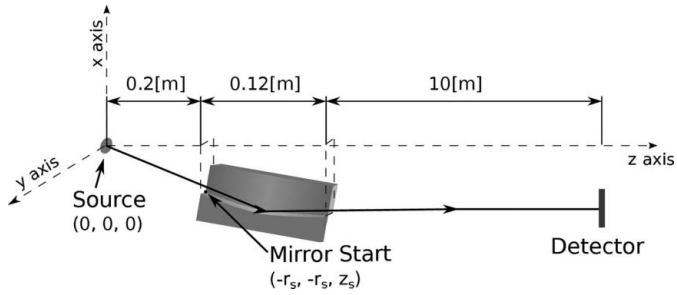

Figure 1
Illustration of the beamline layout used to analyze a collimator application of parabolic nested KB optics.

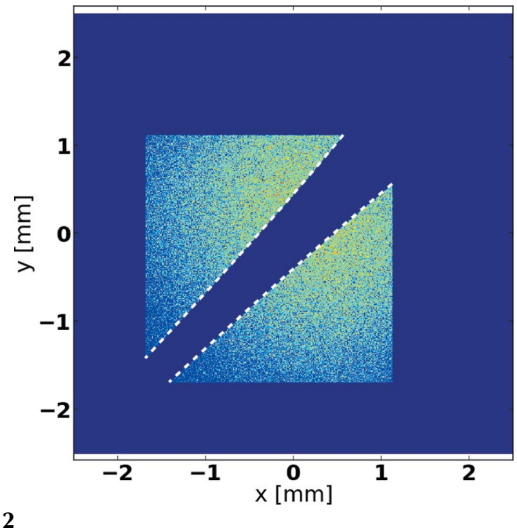

Figure 2
Beam profile obtained with the detector located 10 m from the end of parabolic nested KB optics, with $y_s = 1$ cm, $z_s = 20$ cm and $l = 12$ cm. The source is a point, with Gaussian divergence (FWHM) of 15 mrad. The beam completely covers the optics to better illustrate the output profile. Dashed lines indicate the analytically calculated gap profile, which agrees perfectly with simulation results.

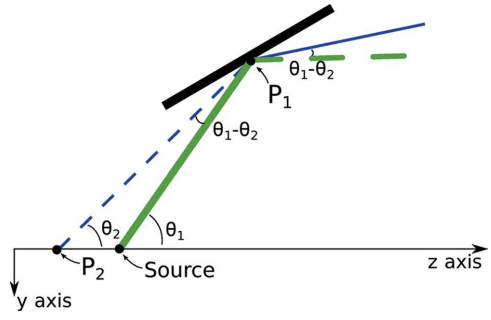

Figure 3
Illustration of the trajectory for a particle that first hits $\mathbf{S}_2$ and then $\mathbf{S}_1$ in the yz plane. The particle begins at the point labeled Source with an angle with the z axis of θ_1 and travels along the thick solid segment until point P_1. At P_1 the particle hits $\mathbf{S}_2$ and is collimated along the x axis, but acquires an angle with the z axis of θ_2 in the yz plane. As a result of this change in direction in the yz plane, the particle appears to the second surface, $\mathbf{S}_1$, as if it originated from P_2, not Source, resulting in an off-axis trajectory. From P_1, the particle follows the thin solid line which is deflected from the z axis by the angle $\theta_1 - \theta_2$. This angle determines the gap in Fig. 2. A similar effect happens in the xz plane for particles that first hit $\mathbf{S}_1$ and then $\mathbf{S}_2$. (The drawing is not to scale for clarity; the angles and the distance between Source and P_2 are exaggerated.)

the two surfaces. Its direction is described by the unit vector of its velocity,

$$\hat{\mathbf{v}} = \begin{pmatrix} v_y & v_y & v_z \end{pmatrix}. \tag{6}$$

Suppose that the particle is bound to hit one of the two surfaces first. Had the particle hit the surface $\mathbf{S}_1$, it would have had an angle with the z axis of

$$\theta_1 = \arctan\left(v_y/v_z\right) \tag{7}$$

and subsequently have been collimated perfectly in the $\mathbf{y}$ direction by the parabolic profile $\mathbf{S}_1$. However, had the particle interacted with $\mathbf{S}_2$ prior to reflecting from $\mathbf{S}_1$, its direction would have become

$$\hat{\mathbf{v}} = \begin{bmatrix} 0 & v_y & (v_y^2 + v_z^2)^{1/2} \end{bmatrix}. \tag{8}$$

Therefore, this particle would hit $\mathbf{S}_1$ with an angle with the z axis of

$$\theta_2 = \arctan\left[\frac{v_y}{(v_y^2 + v_z^2)^{1/2}}\right]. \tag{9}$$

The resulting divergence of the particle from the z axis is

$$\theta_1 - \theta_2 = \arctan\left(\frac{v_y}{v_z}\right) - \arctan\left[\frac{v_y}{(v_y^2 + v_z^2)^{1/2}}\right]. \tag{10}$$

Fig. 3 illustrates the two divergent trajectories. We can express the above equation as a function of the z-axis position of the intersection point where the particle hits the mirror, by using the relation that the position of the particle is related to the velocity by a scalar constant t, $\mathbf{x} = \mathbf{v}t$. The expression becomes

$$\theta_1 - \theta_2 = \arctan\left(\frac{y_\mathrm{h}}{z_\mathrm{h}}\right) - \arctan\left[\frac{y_\mathrm{h}}{(y_\mathrm{h}^2 + z_\mathrm{h}^2)^{1/2}}\right]. \tag{11}$$

Here y_h is the y-axis position of the intersection point where the particle hits, given by

$$y_\mathrm{h}(z_\mathrm{h}) = -2\left[p(z_\mathrm{h} + p)\right]^{1/2}, \tag{12}$$

and z_h is the z-axis position where the particle hits the intersection, whose possible values span the length of the optics:

$$z_\mathrm{s} < z_\mathrm{h} < z_\mathrm{s} + l. \tag{13}$$

Finally, we compute the edge of the gap on a detector at a distance d from the end of the optics, z_e, shown as dashed lines in Fig. 2. For particles that hit the $\mathbf{S}_1$ surface first, the gap edge on the detector is given by

$$[y_\mathrm{d}(z_\mathrm{h}), y_\mathrm{h}(z_\mathrm{h})], \tag{14}$$

whereas for particles that hit the $\mathbf{S}_2$ surface first, the edge is

$$[y_\mathrm{h}(z_\mathrm{h}), y_\mathrm{d}(z_\mathrm{h})]. \tag{15}$$

Since the distance between the detector and the point where the ray hits the mirror is $d + z_\mathrm{e} - z_\mathrm{h}$, then $y_\mathrm{d}(z_\mathrm{h})$ is given by

$$\begin{aligned} y_\mathrm{d}(z_\mathrm{h}) &= y_\mathrm{h} + (d + z_\mathrm{e} - z_\mathrm{h})\tan(\theta_1 - \theta_2), \\ &= y_\mathrm{h} + (d + z_\mathrm{e} - z_\mathrm{h})\tan\left\{\arctan\left(\frac{y_\mathrm{h}}{z_\mathrm{h}}\right)\right. \\ &\quad \left. - \arctan\left[\frac{y_\mathrm{h}}{(y_\mathrm{h}^2 + z_\mathrm{h}^2)^{1/2}}\right]\right\}. \end{aligned} \tag{16}$$

Fig. 2 illustrates the perfect consistency between ray tracing and analytical calculations in determining the gap profile.

4. Determining the correct alignment of nested mirrors

4.1. Optimal alignment condition

A simple argument derives the necessary condition for the collimation of light incident on the intersection between two mirror surfaces.

Let the direction of an on-axis particle which will hit a point along the intersection be given by $\hat{\mathbf{v}}$. Assume that the particle will hit one of the surfaces first and denote the vector normal to the surface at the point of contact as $\mathbf{n}_1$. Following the reflection from this first surface, the direction of the particle becomes

$$\hat{\mathbf{v}}_1 = \hat{\mathbf{v}} - 2\mathbf{n}_1 \cdot \hat{\mathbf{v}}. \tag{17}$$

Now the particle hits the second surface. Denote the vector normal to the second surface at the point of contact as $\mathbf{n}_2$. Following this second reflection, the direction of the particle becomes

$$\hat{\mathbf{v}}_{12} = \hat{\mathbf{v}}_1 - 2\mathbf{n}_2 \cdot \hat{\mathbf{v}}_1. \tag{18}$$

Substituting the expression for $\mathbf{v}_1$ we find

$$\hat{\mathbf{v}}_{12} = \hat{\mathbf{v}} - 2(\mathbf{n}_1 \cdot \hat{\mathbf{v}})\mathbf{n}_1 - 2\left\{\mathbf{n}_2 \cdot \left[\hat{\mathbf{v}} - 2(\mathbf{n}_1 \cdot \hat{\mathbf{v}})\mathbf{n}_1\right]\right\}\mathbf{n}_2. \tag{19}$$

Now consider a counterpart particle which hits the two surfaces in the opposite order. Its final direction would be

$$\hat{\mathbf{v}}_{21} = \hat{\mathbf{v}} - 2(\mathbf{n}_2 \cdot \hat{\mathbf{v}})\mathbf{n}_2 - 2\left\{\mathbf{n}_1 \cdot \left[\hat{\mathbf{v}} - 2(\mathbf{n}_2 \cdot \hat{\mathbf{v}})\mathbf{n}_2\right]\right\}\mathbf{n}_1. \tag{20}$$

Since the order of reflections should not affect the ultimate direction of propagation, the condition for alignment is

$$\hat{\mathbf{v}}_{12} = \hat{\mathbf{v}}_{21}. \tag{21}$$

Substituting the expressions for $\hat{\mathbf{v}}_{12}$ and $\hat{\mathbf{v}}_{21}$, we obtain

$$(\mathbf{n}_1 \cdot \hat{\mathbf{v}})(\mathbf{n}_2 \cdot \mathbf{n}_1)\mathbf{n}_2 = (\mathbf{n}_2 \cdot \hat{\mathbf{v}})(\mathbf{n}_1 \cdot \mathbf{n}_2)\mathbf{n}_1. \tag{22}$$

This equation is satisfied in three different scenarios. The first is if $\mathbf{n}_1 = \mathbf{n}_2$. This is the case in a paraboloid or ellipsoid single-reflection geometry. The second is if both $\mathbf{n}_1$ and $\mathbf{n}_2$ are orthogonal to $\mathbf{v}$. This is the trivial case in which the particle is already collimated and no reflections occur from the surface. Finally, the above condition is satisfied provided that $\mathbf{n}_1$ is orthogonal to $\mathbf{n}_2$:

$$\mathbf{n}_1 \cdot \mathbf{n}_2 = 0. \tag{23}$$

This is the condition of interest for the nested KB mirror geometry. For elliptical or parabolic mirrors this condition cannot be perfectly satisfied at every point simultaneously along the intersection between the two mirrors. However, it is

possible to satisfy the condition exactly at one point along the intersection and to a good approximation at a second point, improving overall the collimating or focusing properties of the optics.

4.2. Rotations for optimal alignment

We choose to enforce equation (23) at the point along the optics where the maximum intensity of light is reflected. We then rotate each individual surface around the normals at this point until the normals at another point along the geometry are approximately orthogonal, such as the end of the mirrors.

Let $\mathbf{T}$ define a matrix of symmetry for the geometry such that, for any point on the first mirror $\mathbf{S}_1$, the equivalent point on the second mirror $\mathbf{S}_2$ is given by

$$\mathbf{S}_2 = \mathbf{T}\mathbf{S}_1. \tag{24}$$

From equations (1) and (2),

$$\mathbf{T} = \begin{pmatrix} 0 & 1 & 0 \\ 1 & 0 & 0 \\ 0 & 0 & 1 \end{pmatrix}. \tag{25}$$

Let $\mathbf{R}$ define the matrix for a rotation by an angle θ around a unit vector $\hat{\mathbf{u}}$ as given by the Rodrigues' formula,

$$\mathbf{R}(\theta, \hat{\mathbf{u}}) = \mathbf{I}\cos\theta + \mathbf{J}(\hat{\mathbf{u}})\sin\theta + (1 - \cos\theta)[\mathbf{J}(\hat{\mathbf{u}})]^2, \tag{26}$$

where $\mathbf{J}(\hat{\mathbf{u}})$ is defined by

$$\mathbf{J}(\hat{\mathbf{u}}) \equiv \begin{pmatrix} 0 & -u_z & u_y \\ u_z & 0 & -u_x \\ -u_y & u_x & 0 \end{pmatrix}. \tag{27}$$

Note that for any vector $\mathbf{x}$,

$$\mathbf{J}(\hat{\mathbf{u}})\mathbf{x} = \hat{\mathbf{u}} \times \mathbf{x}. \tag{28}$$

Let $\mathbf{n}_{c1} = \mathbf{n}_{p1}(z_c)$ denote the vector normal to a surface at the point along the intersection z_c where the most intensity will be incident. First, this vector must be orientated perpendicular to its counterpart on the other surface ($\mathbf{T}\mathbf{n}_{c1}$) by rotating around a vector $\hat{\mathbf{g}}$, which is orthogonal to both. Therefore, the vector to rotate the normal about is given by

$$\hat{\mathbf{g}} = \frac{\mathbf{n}_{c1} \times \mathbf{T}\mathbf{n}_{c1}}{|\mathbf{n}_{c1} \times \mathbf{T}\mathbf{n}_{c1}|}. \tag{29}$$

Since the angle between $\mathbf{n}_{c1}$ and $\mathbf{T}\mathbf{n}_{c1}$ is

$$\sin\theta = |\mathbf{n}_{c1} \times \mathbf{T}\mathbf{n}_{c1}|, \tag{30}$$

$\mathbf{n}_{c1}$ must be rotated about $\hat{\mathbf{g}}$ by

$$\varphi_1 = -\frac{1}{2}\left[\frac{\pi}{2} - \arcsin(|\mathbf{n}_{c1} \times \mathbf{T}\mathbf{n}_{c1}|)\right]. \tag{31}$$

Correspondingly, the rotation matrix is

$$\mathbf{R}_1 = \mathbf{R}(\varphi_1, \hat{\mathbf{g}}). \tag{32}$$

As a result the newly rotated normal at the point of maximum intensity is $\mathbf{R}_1\mathbf{n}_{c1}$.

Next we orient the normals at another point along the optics (such as the end), by rotating around $\mathbf{R}_1\mathbf{n}_{c1}$. Let $\mathbf{k} = \mathbf{R}_1\mathbf{n}_{e1}$ denote the normal (following the first rotation) at this second point. We determine the rotation angle by solving for φ_2 in the following equation:

$$\left[\mathbf{R}(\varphi_2, \mathbf{R}_1\mathbf{n}_{c1})\mathbf{k}\right] \cdot \left[\mathbf{T}\mathbf{R}(\varphi_2, \mathbf{R}_1\mathbf{n}_{c1})\mathbf{k}\right] = 0. \tag{33}$$

Using the small-angle expansions for sine and cosine, a reasonable analytical approximation for the value of φ_2 can be found. This is given by (see Appendix A for the derivation)

$$\varphi_2 = \frac{-(\mathbf{k}\cdot\mathbf{m}) \pm [(\mathbf{k}\cdot\mathbf{m})^2 - (\mathbf{m}\cdot\mathbf{T}\mathbf{m})(\mathbf{k}\cdot\mathbf{T}\mathbf{k})]^{1/2}}{\mathbf{m}\cdot\mathbf{T}\mathbf{m}}, \tag{34}$$

where

$$\mathbf{m} = \mathbf{T}(\mathbf{R}_1\mathbf{n}_{c1} \times \mathbf{k}) \tag{35}$$

and the smaller value in magnitude for φ_2 is the desired value. The second rotation is then given by

$$\mathbf{R}_2 = \mathbf{R}(\varphi_2, \mathbf{R}_1\mathbf{n}_{c1}). \tag{36}$$

Finally, the complete rotation for this surface is

$$\mathbf{R}_{T1} = \mathbf{R}_2\mathbf{R}_1. \tag{37}$$

We can then find the rotation for the second surface with

$$\mathbf{R}_{T2} = \mathbf{T}\mathbf{R}_2\mathbf{R}_1\mathbf{T}. \tag{38}$$

The rotation-matrix formalism is used for simulations of the geometry by the ray-tracing software.

4.3. Orientation of the detector

As a result of these rotations, the direction of propagation of the output beam and the location of the focal point change slightly. Since our simulations determined that the change in the location is small, we can determine the new output propagation direction by noting that, under the orthogonal condition ($\mathbf{n}_{c1}\cdot\mathbf{n}_{c2} = 0$) and for a ray traveling on the symmetric plane ($\hat{\mathbf{v}} = \mathbf{T}\hat{\mathbf{v}}$), equation (19) can be written as

$$\hat{\mathbf{v}}_{12} = \hat{\mathbf{v}} - 2\left[2^{-1/2}(\mathbf{n}_1 + \mathbf{n}_2)\cdot\hat{\mathbf{v}}\right]2^{-1/2}(\mathbf{n}_1 + \mathbf{n}_2). \tag{39}$$

Therefore, letting $\mathbf{v}$ be a ray traveling from the source to the center of the optics, and $\mathbf{n}_1$ and $\mathbf{n}_2$ be the rotated normals of the mirrors taken at the point of maximum intensity, it is straightforward to determine the direction of propagation of the output beam. This propagation direction can then be used to correctly situate the detector relative to the optics.

4.4. Determining the shape of the mirror substrate blocks

Fig. 4 shows the geometry of the substrates that form the rotated nested KB mirrors. The substrates are cut to ensure optimal alignment as described above. The determined surface orientation can be achieved by cutting the sides and bottom of the substrate by the appropriate angles θ_s and θ_b which are determined from the rotation matrix using the following procedure. Let $\mathbf{p}$ be the unit eigenvector of the symmetric matrix $\mathbf{T}$, identified by

$$\mathbf{p} = -\mathbf{T}\mathbf{p} = \begin{pmatrix} -1 & 1 & 0 \end{pmatrix}. \tag{40}$$

The angles made by the sides θ_s and bottom θ_b of the blocks are then given by

$$\theta_s = \arctan\left(\frac{\hat{\mathbf{b}}\cdot\mathbf{R}_{T1}^{-1}\mathbf{p}}{\hat{\mathbf{h}}\cdot\mathbf{R}_{T1}^{-1}\mathbf{p}}\right), \quad \theta_b = \arctan\left(\frac{\hat{\mathbf{b}}\cdot\mathbf{R}_{T1}^{-1}\mathbf{p}}{\hat{\mathbf{l}}\cdot\mathbf{R}_{T1}^{-1}\mathbf{p}}\right), \tag{41}$$

where $\hat{\mathbf{b}}$, $\hat{\mathbf{h}}$ and $\hat{\mathbf{l}}$ are the unit vectors along the base, height and length of the block respectively, in their unrotated state and $\mathbf{R}_{T1}^{-1}$ is the inverse of the alignment matrix for the surface.

5. Simulation of parabolic collimation optics for inverse Compton sources

5.1. Simulating a laterally graded multilayer mirror coating

Throughout our simulations, the parabolic surfaces composing the optics were simulated as being coated with a laterally graded multilayer formed by 100 bilayers of W/Si, where the ratio of the thickness of the silicon layer to total bilayer thickness is

$$\Gamma = 0.8. \tag{42}$$

A suitable approximation to the ideal profile of the bilayer thickness (d) can be derived using Bragg's law corrected for refraction, given by

$$d(z) = \frac{\lambda}{2\{\sin^2\left[\theta_g(z)\right] - 2\delta\}^{1/2}}. \tag{43}$$

Here λ is the average expected wavelength, $\theta_g(z)$ is the average expected incident grazing angle and δ is the mean decrement in reflectivity, given by

$$\delta = (1-\Gamma)\Re\{1-n_1\} + \Gamma\Re\{1-n_2\}, \tag{44}$$

where n_1 and n_2 are the complex refractive indexes for the top and bottom bilayer materials, respectively, and $\Re\{\ldots\}$ denotes the real part. The complex refractive index of a material can be calculated from the scattering length using (Als-Nielsen & McMorrow, 2011)

$$n_i = 1 - \frac{\lambda^2\Re\{b_i\}}{2\pi} + i\frac{\lambda\Im\{b_i\}}{4\pi}, \tag{45}$$

where λ is the average expected wavelength and b_i is the scattering length density. For the W and Si materials used through our simulations, these values are given by, at $\lambda = 1.54051$ Å,

$$b_1 = 4.678[\text{Å}^{-3}]r_0 + i33.235\times10^{-6}[\text{Å}^{-2}], \tag{46}$$

$$b_2 = 0.699[\text{Å}^{-3}]r_0 + i1.399\times10^{-6}[\text{Å}^{-2}], \tag{47}$$

where b_1 is the complex index for tungsten (W), b_2 is the complex index for silicon (Si) and r_0 is the classical Thompson scattering length.

Using equation (1) for $\mathbf{S}_{p1}$ it is straightforward to determine an expression for the expected incident grazing angle at a particular point along the surface $\theta_g(z)$ for the parabola geometry:

$$\theta_g(z) = \frac{1}{2}\arctan\left\{\frac{-2[p(z+p)]^{1/2}}{z}\right\}. \tag{48}$$

Within our simulations, the reflectivity of the multilayers was calculated using the Parratt formula (Als-Nielsen & McMorrow, 2011). The surfaces were simulated without any roughness or figure error. Fig. 5 illustrates the variation in the multilayer thickness across the surface of the mirror.

5.2. Simulation results

Both ray-tracing simulation and analytical considerations show that the best performing geometry results from minimizing y_s and z_s and maximizing the length of the optics l. Minimizing y_s and z_s is subject to the physical constraints of the source and the maximum grazing angle of the material ($\theta_g \simeq 24$ mrad for W/Si), while maximizing the length of the optics l is subject to manufacturing limitations. For our setup,

$$z_s = 0.2\,\text{m}, \quad y_s = -z_s\sin(2\theta_{gmax}) = -0.0096\,\text{m}, \tag{49}$$

corresponding to a parabolic parameter of

$$p = 1.151\times10^{-4}\,\text{m}. \tag{50}$$

Using the source parameters described in §2, we proceeded to scan the throughput of the optics as a function of length. Fig. 6 illustrates the mirror throughput at the detector as a function of the length of the mirror.

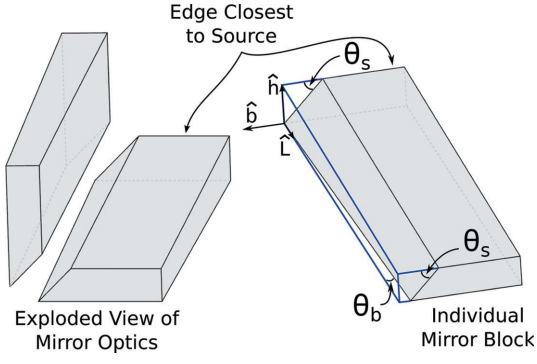

Figure 4
Illustration depicting the exploded view of the optics (left) along with the angles θ_b and θ_s for a single mirror block (right). The local coordinate unit vectors $\hat{\mathbf{b}}$, $\hat{\mathbf{h}}$ and $\hat{\mathbf{L}}$ are likewise shown.

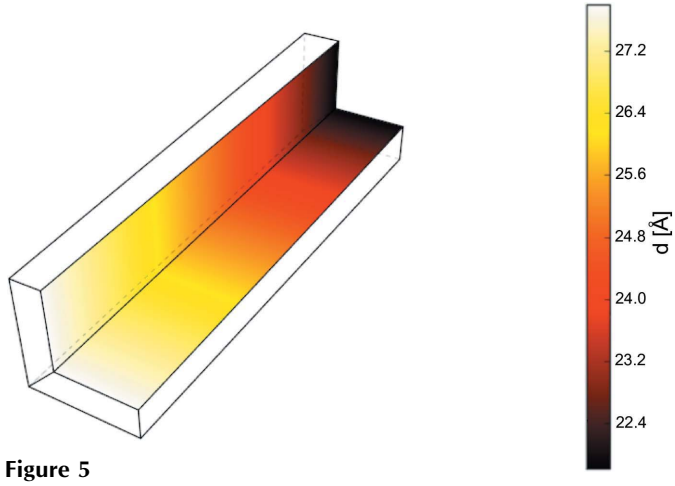

Figure 5
Plot of the variation of the bilayer thickness (d) across the surfaces of the mirror. The source is located in the direction of the upper right corner. The minimum bilayer thickness is 21.817 Å, while the maximum thickness is 27.804 Å.

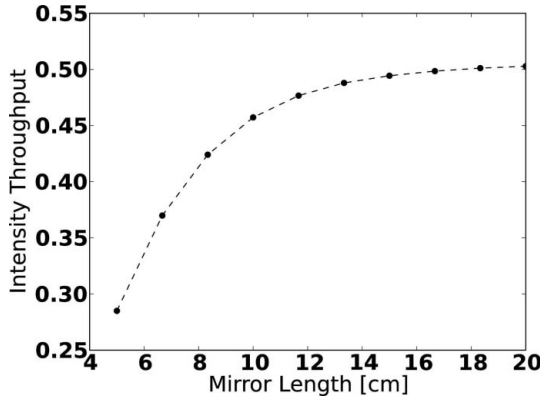

Figure 6
Intensity at the detector as a function of mirror length for designs with $y_s = -0.0096$ m and $z_s = 0.2$ m.

Taking practical manufacturing limits into account, we decided on a design with a mirror length of $l = 0.12$ m, corresponding to a throughput of 0.478.

Fig. 7 compares the output of the beam using this mirror design for the various levels of corrective rotations of the optics. The profile of the beam using both the first and second rotations (Fig. 7*c*) corresponds to a Gaussian-like distribution with a spacial FWHM of ∼0.7 mm and a half-divergence of ∼0.01 mrad.

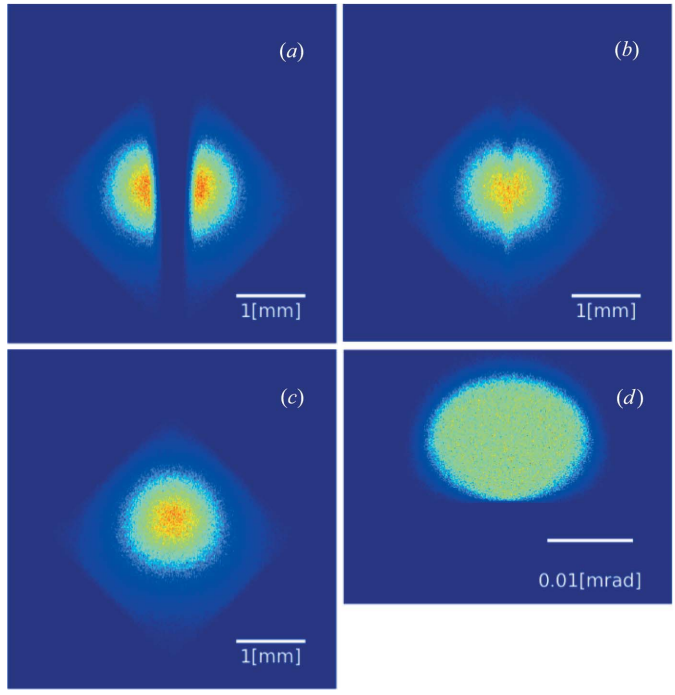

Figure 7
Comparison of corrections at 10 m from the end of the optics for a 0.12 m-long design using a Gaussian source with an energy of 12 keV, a radius of 2.5 µm and an FWHM divergence of 5 mrad. (*a*) No rotation, (*b*) only first rotation, and (*c*) first and second rotation. (*d*) is a plot of the *x*-axis and *y*-axis divergence using the first and second rotation. The throughput of the optics for all of the above plots is 0.478.

6. Discussion

The propagation of two reflected beams and the gap between them shown in Fig. 1 are specific to Montel optics. Two divergent pathways through the optics appear because a ray could be reflected from either the horizontal or the vertical mirror first. To correct this divergence, the mirrors must be tilted and rotated such that the two rays propagate in the same direction after the second reflection. Elliptical Montel optics, such as for nanoprobe applications, were not considered here in detail, but the same condition $\mathbf{v}_{12} = \mathbf{v}_{21}$ should be satisfied for the beam to form a single focal point. The mirror rotation and detector position should be determined by a similar method.

Standard KB mirrors, which consist of sequential horizontal and vertical mirrors, do not produce two divergent rays, since all the rays follow the same order of reflections.

For practical purposes, ray-tracing simulations must take into account imperfections of the optics, including figure errors, roughness and misalignment between the mirrors. These effects will have to be studied separately, but they should have a similar effect on the performance of Montel optics as they do on standard KB mirrors.

The technological challenge specific to Montel geometry is the precision cutting of mirrors near the corner, where the center of the beam is located. This is different from KB mirrors, where the center of the beam strikes away from the mirror's edges. However, we expect that Montel optics could be made to the same angular resolution as KB mirrors, allowing the use of Montel mirrors for applications such as crystallography, SAXS, and nanoprobe at both synchrotron beamlines and compact X-ray sources, as well as neutron applications.

In summary, we have developed an analytical description of nested KB mirrors, including their shapes and mutual orientation. We found that the correct orientation of mirrors with respect to each other is not perpendicular, as was assumed previously. In fact, we showed analytically and by ray-tracing simulations that, after reflections from two perpendicular nested mirrors, the beam would split into two nonparallel beams downstream from the optics. This effect is due to the difference in optical paths of particles that are reflected initially from different mirrors. As an example, we considered parabolic mirrors and derived the mutual orientation angles of the mirrors for producing an almost parallel beam after the optics. The application of the nested KB optics as a collimator for a compact X-ray source (Graves *et al.*, 2014) is discussed in detail.

APPENDIX *A*
Derivation of analytical approximation of the second rotation angle

An analytical approximation for the second rotation angle φ_2 can be derived in the limit where $\varphi_2 \ll 1$. Using equation (26), along with the small-angle approximations

$$\sin\varphi_2 \cong \varphi_2, \quad \cos\varphi_2 \cong 1, \tag{51}$$

we note that equation (36) reduces to

$$\mathbf{R}_2 = \mathbf{R}(\varphi_2, \mathbf{R}_1\mathbf{n}_{c1}) \cong \mathbf{I} + \varphi_2\mathbf{J}(\mathbf{R}_1\mathbf{n}_{c1}). \quad (52)$$

Hence,

$$\mathbf{R}_2\mathbf{k} \cong \mathbf{k} + \varphi_2\mathbf{J}(\mathbf{R}_1\mathbf{n}_{c1})\mathbf{k} \cong \mathbf{k} + \varphi_2(\mathbf{R}_1\mathbf{n}_{c1}) \times \mathbf{k}, \quad (53)$$

where we have used the property that

$$\mathbf{J}(\hat{\mathbf{u}})\mathbf{x} = \hat{\mathbf{u}} \times \mathbf{x}. \quad (54)$$

Using the above result for $\mathbf{R}_2$ with equation (34) we find

$$\begin{aligned} 0 &= \left[\mathbf{R}(\varphi_2, \mathbf{R}_1\mathbf{n}_{c1})\mathbf{k}\right] \cdot \left[\mathbf{T}\mathbf{R}(\varphi_2, \mathbf{R}_1\mathbf{n}_{c1})\mathbf{k}\right] \\ &= \left\{\mathbf{I} + \varphi_2[(\mathbf{R}_1\mathbf{n}_{c1}) \times \mathbf{k}]\right\} \cdot \left(\mathbf{T}\left\{\mathbf{I} + \varphi_2[(\mathbf{R}_1\mathbf{n}_{c1}) \times \mathbf{k}]\right\}\right) \\ &= \mathbf{k} \cdot \mathbf{T}\mathbf{k} + 2\varphi_2\mathbf{k} \cdot \left\{\mathbf{T}\left[(\mathbf{R}_1\mathbf{n}_{c1}) \times \mathbf{k}\right]\right\} \\ &\quad + \varphi_2^2\left[(\mathbf{R}_1\mathbf{n}_{c1}) \times \mathbf{k}\right] \cdot \left\{\mathbf{T}\left[(\mathbf{R}_1\mathbf{n}_{c1}) \times \mathbf{k}\right]\right\}. \end{aligned} \quad (55)$$

Letting $\mathbf{m} = \mathbf{T}[(\mathbf{R}_1\mathbf{n}_{c1}) \times \mathbf{k}]$, this simplifies to

$$0 = \mathbf{k} \cdot \mathbf{T}\mathbf{k} + 2\mathbf{k} \cdot \mathbf{m}\varphi_2 + \mathbf{m} \cdot \mathbf{T}\mathbf{m}\varphi_2^2, \quad (56)$$

which is quadratic in φ_2. Hence,

$$\varphi_2 = \frac{-(\mathbf{k} \cdot \mathbf{m}) \pm [(\mathbf{k} \cdot \mathbf{m})^2 - (\mathbf{m} \cdot \mathbf{T}\mathbf{m})(\mathbf{k} \cdot \mathbf{T}\mathbf{k})]^{1/2}}{\mathbf{m} \cdot \mathbf{T}\mathbf{m}}, \quad (57)$$

agreeing with equation (34).

APPENDIX *B*
Simulation software

To allow for the simulation of graded multilayer materials and provide a more modular ray tracer, a Monte Carlo simulation package was written. While the main simulation code was implemented in C++ for improved performance, a Python wrapper enables simulations to be specified from the more user-friendly Python interpreter.

Internally, the software is a general purpose particle tracer consisting of classes representing sources, objects, materials and scenes. To specify a beamline, instances of sources and objects are added to a scene class. During the simulation, the scene calls the source to generate a series of particles. The scene then determines which object is first along the trajectory of a particle by asking for the interaction times from each object. The object with the smallest interaction time is asked to modify the state of that particle to simulate the ensuing event. As a result of this general particle collision routine, the code is able to accurately simulate nested components like the Montel mirror optics in our study.

For greater flexibility, materials are handled independently from the definition of objects. Many objects (such as mirrors) require a material class instance as an initialization parameter. When the scene class asks these objects to handle a particle, they simply move the particle to the point of interaction and then forward the request to the specified material along with the coordinates of the interaction in the component coordinate system. The material class then performs any additional modifications to the particle's state that result from the interaction. This mechanism was devised not only to reduce the amount of code required to define a new material, but also to allow for a single definition of a material to be used with different objects. Graded multilayer coatings can be easily implemented by simply defining a material whose reflectivity varies as a function of the location of the interaction in the component coordinate system.

The development of the ray-tracing software was partially supported by the US Department of Energy, Office of Basic Energy Sciences, Division of Materials Sciences and Engineering, under award DE-FG02-09ER46556.

References

Als-Nielsen, J. & McMorrow, D. (2011). *Refraction and Reflection From Interfaces*, pp. 69–112. Hoboken: John Wiley and Sons.
Graves, W. S., Bessuille, J. *et al.* (2014). *Phys. Rev. ST Accel. Beams*, **17**, 120701.
Graves, W., Brown, W., Kaertner, F. & Moncton, D. (2009). *Nucl. Instrum. Methods Phys. Res. Sect. A*, **608**, S103–S105.
Honnicke, M. G., Keister, J. W., Conley, R., Kaznatcheev, K., Takacs, P. Z., Coburn, D. S., Reffi, L. & Cai, Y. Q. (2011). *J. Synchrotron Rad.* **18**, 862–870.
Ice, G. E., Pang, J. W., Tulk, C., Molaison, J., Choi, J.-Y., Vaughn, C., Lytle, L., Takacs, P. Z., Andersen, K. H., Bigault, T. & Khounsary, A. (2009). *J. Appli. Cryst.* **42**, 1004–1008.
Liu, W., Ice, G. E., Assoufid, L., Liu, C., Shi, B., Zschack, P., Tischler, J., Qian, J., Khachartryan, R. & Shu, D. (2011). *Nucl. Instrum. Methods Phys. Res. Sect. A*, **649**, 169–171.
Weichselbaumer, S., Brandl, G., Georgii, R., Stahn, J., Panzner, T. & Böni, P. (2014). *arXiv*:1406.1313.